

Topological Signature of Stratospheric Poincaré – Gravity Waves

Weixuan Xu^a, Baylor Fox-Kemper^a, Jung-Eun Lee^a, J. B. Marston^b, Ziyang Zhu^c

¹ ^a *Department of Earth, Environment and Planetary Science, Brown University, Providence RI*
² *02912 USA,* ^b *Department of Physics and Brown Theoretical Physics Center, Brown University,*
³ *Providence, RI 02912-S USA,* ^c *Stanford Institute for Materials and Energy Sciences, SLAC*
⁴ *National Accelerator Laboratory, Menlo Park, CA 94025, USA*

arXiv:2306.12191v2 [physics.ao-ph] 7 Jul 2023

⁵ *Corresponding author:* Weixuan Xu, weixuan_xu@brown.edu

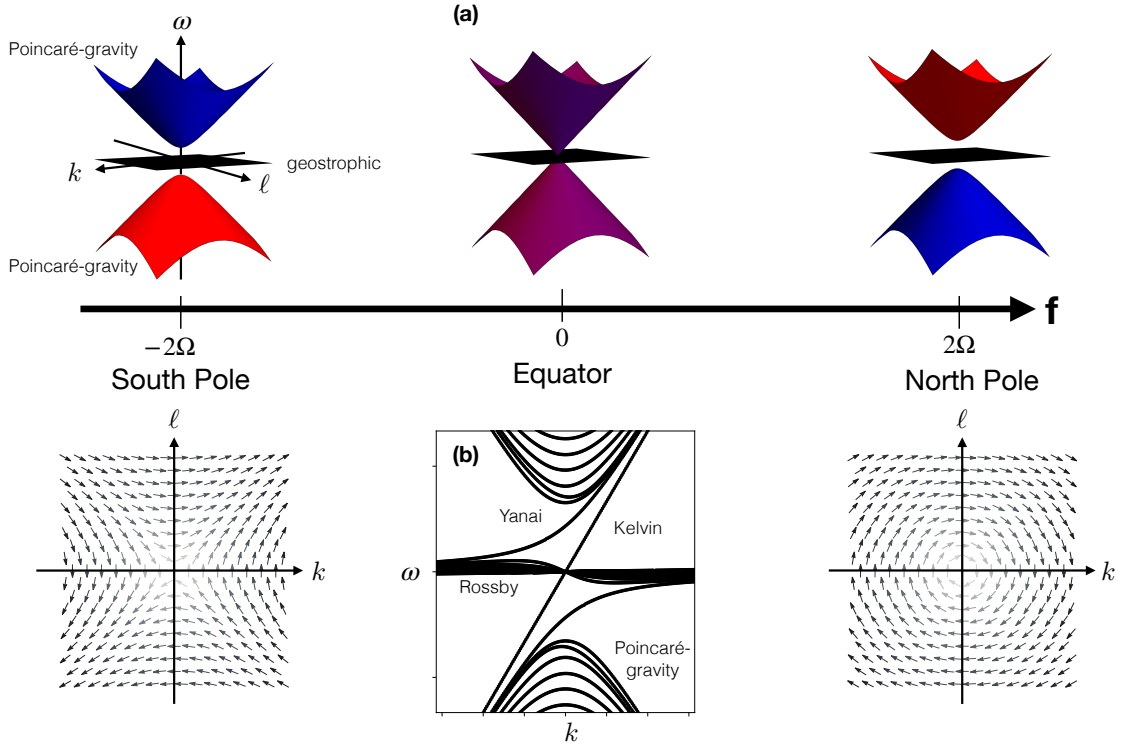
6 ABSTRACT: The rotation of the earth breaks time-reversal and reflection symmetries in an op-
7 posite sense north and south of the equator, leading to a topological origin for certain atmospheric
8 and oceanic equatorial waves. Away from the equator the rotating shallow water and stably strat-
9 ified primitive equations exhibit Poincaré inertio-gravity waves that have nontrivial topology as
10 evidenced by their strict superinertial timescale and a phase singularity in frequency-wavevector
11 space. This non-trivial topology then predicts, via the principle of bulk-interface correspondence,
12 the existence of two equatorial waves along the equatorial interface, the Kelvin and Yanai waves. To
13 directly test the nontrivial topology of Poincaré-gravity waves in observations, we examine ERA5
14 reanalysis data and study cross-correlations between the wind velocity and geopotential height of
15 the mid-latitude stratosphere at the 50 hPa height. We find the predicted vortex and anti-vortex in
16 the relative phase of the geopotential height and velocity at the high frequencies of the waves. By
17 contrast, lower-frequency planetary waves are found to have trivial topology also as expected from
18 theory. These results demonstrate a new way to understand stratospheric waves, and provide a new
19 qualitative tool for the investigation of waves in other components of the climate system.

1. Introduction

Much of what we understand about the climate system is made possible by recognizing the importance of waves in Earth's atmosphere and oceans. Waves are characterized by predictable periodic motion that contrasts with the chaotic or stochastic behavior displayed by many other components of the climate system. Waves are usually categorized dynamically by matching observed variability to predicted dispersion relations (e.g., Wheeler and Kiladis 1999; Farrar 2008), which relate the frequencies and spatial scales where waves may occur and how they propagate through space and time. The phase of waves receive rather less frequent attention. Phasing in the meteorological context refers to different disturbances such as fronts and low-level jets coming together in space and time. Another example in the context of baroclinic instability theory is counterpropagating Rossby waves (Hoskins et al. 1985). Some rogue ocean waves may result from the constructive superposition of multiple smaller waves. Here we demonstrate a different distinguishing and qualitative feature of certain waves, nontrivial topology, that can also be discerned from observations of relative wave phase. The nontrivial topology found here in reanalysis data of stratospheric waves agrees with a recent theoretical prediction of Delplace et al. (2017).

Remarkably, oceanic and atmospheric waves share fundamental physics with those in quantum matter, and topology plays an important role in the movement of the atmosphere and oceans. Although the basic equations for idealized equatorial plane waves in the atmosphere and ocean have been long known (see the historical perspective in Hendershott and Munk 1970) and wavelike variability has been observed in the atmosphere (Wheeler and Kiladis 1999) and ocean (Farrar 2008) with the waves linked to phenomena such as El Niño (Wyrki 1975) and the Madden-Julian Oscillation (Madden and Julian 1971), the connection of waves to topology has only recently been discovered (Delplace et al. 2017). This discovery presents an opportunity to use more sophisticated statistical and mathematical analysis of the wave-like aspects of these phenomena, sharpening our insights into their emergence from diverse variability, fundamental mechanisms, and especially the ability of our modeling systems to appropriately simulate them.

Topology is the field of mathematics concerned with the properties of spaces that do not change under continuous deformations. A doughnut and an orange are topologically distinct because the doughnut has a single hole (we say that it has a genus of 1) while the orange has a genus of 0.



20 FIG. 1. (a) Dispersion relation in frequency-wavevector space for the rotating shallow water equations
 21 in the f-plane approximation as a function of latitude. The upper and lower bands are positive and negative
 22 superinertial frequency modes of the Poincaré waves, and the color indicates the sign of the winding number of
 23 the upper band (blue = -1, red = +1) as shown by the plots of the relative phase difference between the height
 24 and meridional velocity in the lower half of the figure (argument of $\Xi(k, \ell)$; see text). At the equator $f = 0$,
 25 the frequency gap vanishes at a Weyl point, and a topological transition occurs (purple) as the two bands invert.
 26 The subinertial range has only a zero frequency band (black) containing modes in geostrophic balance as there
 27 is no β effect in the f-plane approximation. The inset (b) shows the equatorial β -plane dispersion relations with
 28 the subinertial quasi-geostrophic Rossby waves, the superinertial Poincaré inertio-gravity waves, and the Kelvin
 29 and Yanai waves. Vector plots correspond to the southern hemisphere (left) and the northern hemisphere (right)
 30 respectively.

Likewise a coffee mug has the doughnut topology because it too has a single hole (the handle). Another example, more closely connected to the phenomena discussed below, is known as the Hairy Ball or Hedgehog Theorem that says that it is impossible to comb the spines of a hedgehog (because there will always be at least one tuft) (Renteln 2013). By contrast, if hedgehogs had a

toroidal shape instead of spherical, their spines could be combed smoothly without any bald spots – but probably only boring hedgehogs would choose that hairstyle.

Topology is a powerful tool because it turns complicated problems into simple ones. For example, across an interface between topologically distinct states of matter, a general principle known as bulk-boundary or bulk-interface correspondence (Hasan and Kane 2010) guarantees the existence of boundary or interfacial waves (Fig. 1 (a)). The waves move in one direction and evidence *topological protection*, or immunity to backscattering even in the presence of defects. On a rotating planet, the equator acts as the boundary between two topologically-distinct hemispheres, and so some equatorial waves propagate only in one direction and are topologically protected (Fig. 1 (b)). Past uses of topology in fluid mechanics have usually focused on coherent structures in space such as vortices. Here by contrast we study topology in wavevector-frequency space where it can for instance guarantee the existence of eastward propagating equatorial waves in Earth’s climate system (Delplace et al. 2017). In particular there is a topological origin for two well-known equatorially trapped waves, the Kelvin and Yanai modes, caused by the breaking of time-reversal symmetry by Earth’s rotation, that helps to explain the robustness of these waves against buffeting by the weather. This resilience may also be implicated in other emergent equatorial wavelike phenomena such as the Madden-Julian Oscillation (MJO), remarkable for its eastward propagation along the equator.

Fig. 1a shows the dispersion relation for the idealized rotating shallow-water model on the f -plane. There are three distinct bands: Positive and negative frequency Poincaré-gravity waves (often referred to as “inertio-gravity waves”) and a zero-frequency geostrophically balanced mode. The topology of each band is distinct and may be quantified in terms of a winding number (defined below) in frequency-wavevector space (Horsley 2022). In particular, the Poincaré-gravity modes are characterized by a vortex with winding number of ± 1 . A winding number of $+1$ means that the phase of the complex-valued quantity $\Xi(k, \ell)$ (defined below) increases by 2π as one moves around the center of the vortex in a counter-clockwise direction in wavevector space. The sign of the winding number depends on the sign of the product of the Coriolis parameter and the wave frequency. Geostrophically balanced modes (that become Rossby waves once the Coriolis parameter is allowed to vary with latitude) are by contrast topologically trivial with zero winding number.

Evidently the winding number of the Poincaré-gravity waves changes by 2 upon crossing the equator where the Coriolis parameter changes sign; this is known as “band inversion.” By bulk-interface correspondence, there must therefore be 2 waves that traverse the otherwise forbidden region of frequency space. Spectral flow in frequency-wavevector space as the zonal wavenumber increases shows that the negative frequency Poincaré band loses two modes, the geostrophic band gains and loses one mode and the positive frequency Poincaré band gains the two modes. These are the equatorial Kelvin and Yanai waves. The two equatorial modes move with an eastward group velocity at all zonal wavenumbers, and this unidirectional propagation reflects the breaking of time-reversal invariance by the planetary rotation.

The organization of the rest of the paper is as follows. In Sec. 2 we review the mathematics of topology in the context of the rotating shallow water equations on the f-plane. Sec. 3 discusses the atmospheric ERA5 reanalysis data and its processing into spectral space. Topological properties of waves discerned from the data are presented in Sec. 4 and some conclusions are presented in Sec. 5. Matlab code that we use is included in the Appendix.

2. Theoretical Motivation

To motivate our investigation of the topology of waves in the stratosphere we briefly review the linearized rotating shallow water equations on the f-plane following Delplace et al. (2017).

$$\begin{cases} \frac{\partial u}{\partial t} - f_0 v = -g \frac{\partial h}{\partial x} \\ \frac{\partial v}{\partial t} + f_0 u = -g \frac{\partial h}{\partial y} \\ \frac{\partial h}{\partial t} + H \left(\frac{\partial u}{\partial x} + \frac{\partial v}{\partial y} \right) = 0 \end{cases} \quad (1)$$

Here u and v are the zonal and meridional velocity, f_0 is the Coriolis parameter in the f-plane approximation and g is the gravitational acceleration. Also h is the height anomaly and H is the average depth of the shallow water. Despite the highly idealized nature of these equations, the robustness of topology against continuous deformations means that lessons learned from these equations may be expected to hold in more realistic settings (Zhu et al. 2021).

By adopting periodic boundary conditions to eliminate any boundaries, the normal modes of the linearized rotating shallow water equations may be easily found by Fourier transfor-

mation to frequency-wavevector space followed by diagonalization of a 3×3 matrix. Introducing the 3-component vector $\Psi(x, y, t) \equiv (u(x, y, t), v(x, y, t), h(x, y, t))$ and substituting $\Psi(x, y, t) = \tilde{\Psi}(k, \ell, \omega) e^{i(\vec{k} \cdot \vec{x} - \omega t)}$ with $\vec{k} = (k, \ell)$, we obtain

$$\begin{bmatrix} -i\omega & -f_0 & igk \\ f_0 & -i\omega & ig\ell \\ iHk & iH\ell & -i\omega \end{bmatrix} \times \begin{bmatrix} \tilde{u} \\ \tilde{v} \\ \tilde{h} \end{bmatrix} = 0 \quad (2)$$

This secular equation is solved to obtain three normal mode angular frequencies of $\omega_{\pm} = \pm \sqrt{gH(k^2 + \ell^2) + f_0^2}$ and $\omega_0 = 0$. In the long-wavelength limit ($f_0^2 \gg gH(k^2 + \ell^2)$) the amplitudes of the positive and negative frequency Poincaré-gravity waves are:

$$\tilde{\Psi}_{\pm} = \begin{bmatrix} \pm(k \pm i\ell \operatorname{sgn}(f_0))|f_0| \\ -i(k \pm i\ell \operatorname{sgn}(f_0))f_0 \\ H(k^2 + \ell^2) \end{bmatrix} \quad (3)$$

up to an overall normalization. Note that $\Psi_{\pm}^*(\vec{k}, f_0) = \Psi_{\pm}(\vec{k}, -f_0)$ whereas the positive and negative frequency modes are related by band inversion $\Psi_{-}(\vec{k}, f_0) = \Psi_{+}(-\vec{k}, -f_0)$. The presence of the $k \pm i\ell \operatorname{sgn}(f_0)$ term signals the appearance of a phase singularity at the origin in wavevector space.

Normal modes are defined only up to an overall phase and magnitude. To quantify their topology we follow Zhu et al. (2021) by introducing a gauge-invariant but complex-valued quantity Ξ defined as follows:

$$\Xi(k, \ell) \equiv h^*(k, \ell) v(k, \ell). \quad (4)$$

We say that Ξ is gauge-invariant because the overall phase of the normal modes cancels out; only the relative phase difference between two components of the waves (in this case, meridional velocity and height) remains. A Fourier transform of Ξ into real space and time reveals it to be a cross-correlation between two field points that are separated in space and time. As waves propagate simultaneously in both space and time it is perhaps not surprising that non-local correlations play a role in their topological classification.

In the case of the superinertial Poincaré-gravity waves the gauge-invariant quantity displays a vortex or antivortex (depending on the signs of the frequency and the Coriolis frequency) centered at the origin in wavevector space:

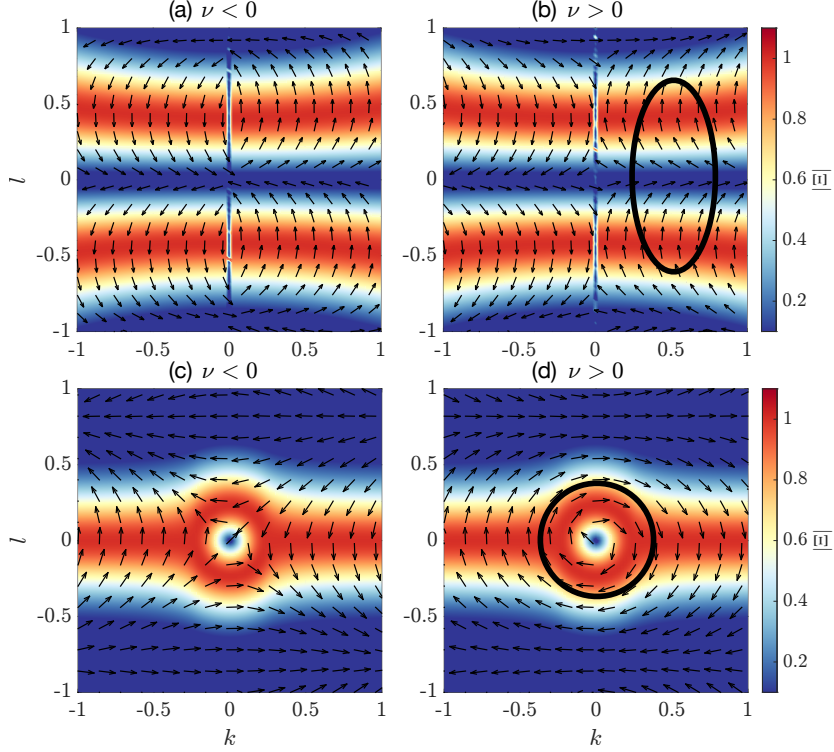
$$\Xi_{\pm}(k, \ell) = -iH f_0(k^2 + \ell^2)(k \pm i\ell \operatorname{sgn}(f_0)) \quad (5)$$

In the northern hemisphere, $f_0 > 0$, and the positive-frequency waves have winding number $+1$ whereas negative-frequency waves have winding number -1 ; these topological charges are reversed in the southern hemisphere (the bands invert). The related product $h^*(k, \ell) u(k, \ell)$ involving the zonal velocity exhibits the same winding numbers. The zero-frequency geostrophic mode, by contrast, has (up to multiplication by a real-valued normalization constant) the following form:

$$\Xi_0(k, \ell) = ig f_0 k \quad (6)$$

and thus has a domain wall at $k = 0$ and zero winding number. Its topological charge therefore vanishes. The same result may be obtained from the barotropic quasigeostrophic equations as the wave height is proportional to the stream function while the meridional velocity is proportional to the zonal derivative of the stream function thus leading in wavevector space to the same form as Eq. 6.

Representing the relative phase Ξ with an arrow makes these patterns evident as shown in Figure 2. In Delplace et al. (2017) and many other papers, linearized wave equations have been characterized in terms of the topological Chern number. However the Chern number has several disadvantages. First, in contrast to systems on spatial lattices (where the Chern number was first applied), for continuous systems the Chern number need not be integer and its value depends on how an integral over the Berry curvature is regularized at high wavevectors. This ambiguity can sometimes be avoided by compactification (Delplace et al. 2017; Venaille and Delplace 2021). Here we point out that this is more of a mathematical problem than a physical one because at small scales dissipation is important and ultimately at the smallest scales the fluid description breaks down entirely and is replaced by discrete molecular dynamics. In any case the ambiguity does not arise for the winding number which is determined at finite wavevectors. Second, it is unclear how to extend the Chern number to systems with dissipation, driving, or nonlinearities – all properties



31 FIG. 2. Theoretical calculation of the cross-correlation $\Xi(k, \ell)$ for normal modes at (a)-(b) low frequencies
 32 (Rossby waves) and (c)-(d) high frequencies (Poincaré-gravity waves). Here, we perform the calculation for the
 33 northern hemisphere with a spatially varying Coriolis parameter to lift the degeneracy of the geostrophic mode:
 34 $f(y) = 1 + 0.5 \sin(2\pi y/L_y)$, where $L_y = 10\pi$ is the domain size. See Zhu et al. (2021) for details. Plots (a) and
 35 (c) show the negative frequency modes, and (b) and (d) are for positive frequencies. The color bar represents
 36 the magnitude of Ξ and the arrows show the phase of its complex value. The low-frequency planetary waves
 37 have a domain wall at $k = 0$ and are topologically trivial as a closed path that avoids the $\Xi = 0$ domain wall
 38 has zero winding number (black oval). While the cross-correlation structure of the geostrophic mode in (a)-(b)
 39 depends on the choice of normal modes, the winding number remains zero for all modes. Note that the winding
 40 number of the high-frequency Poincaré-gravity waves (black circle in the bottom figure) depends on the sign of
 41 the frequency of the waves.

of geophysical fluids. Finally it is difficult to compute the Chern number from observations or
 simulations because it involves an integral of the Berry curvature over wavevector space. We note
 that the winding number has recently been utilized in a number of different contexts including
 active optical media (Bouteyre et al. 2022).

3. Methods

To use observations to find topological winding numbers by following the approach described above requires high sampling rates, greater than 1 cycle per day (CPD), at many spatial points over a large region. Measurements of the ocean have been performed over large regions at low sampling rates, and separately at isolated locations at high rates, but not both simultaneously. We therefore turn to the stratosphere and avoid for now the troposphere as it is generally less stably stratified and subjected to orographic effects and baroclinic and convective instabilities. We make use of the ERA5 reanalysis data set which contains high-frequency data sampled evenly over the globe. Later in the Sec. 5 we sketch a possible way to avoid the requirement for a fine spatial grid of data points.

a. Reanalysis Data

In order to investigate the topology of the Poincaré-gravity waves from the observation, the velocity and geopotential height fields (u, v, h) should satisfy two conditions. First, the region to be studied should be several deformation lengths away from the equator to ensure that the waves are not strongly influenced by equatorially-trapped waves. In the language of topological physics this is the “bulk” region. Second the data sampling interval should be short enough to resolve signals with a frequency of up to 2 CPD. Following Pahlavan et al. (2021) who diagnosed the equatorial Kelvin and Yanai waves as well as Poincaré-gravity waves in spectral analysis of the stratosphere, we use ERA5 reanalysis data (Hersbach et al. 2020) at the 50 hPa level. We sample the horizontal components of the velocity and the geopotential heights at 6 hour intervals over the period of 1981 to 2020. The spatial domain ranges from from 25°N to 65°N across all longitudes with a horizontal resolution of 0.25°.

b. Data Processing

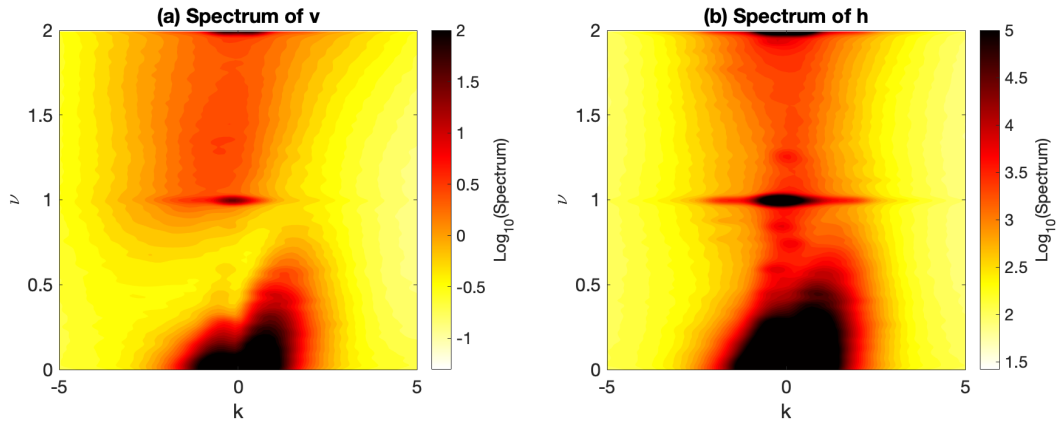
To work with a manageable data set size, we first reduce the spatial resolution by interpolating the variables to a coarser resolution of 1° in latitude and 2.5° in longitude. As the Poincaré-gravity waves that we wish to study have long wavelengths this reduction in resolution does not affect the analysis. Next we remove the seasonal signals from the data by first applying a low-pass boxcar filter with a window of 182 days (half of a year) in the time dimension to isolate the

low-frequency component, and then subtract that from data, leaving only the high frequency components. Poincaré-gravity waves appear at frequencies that exceed the local pendulum frequency. For a latitude of $\phi = 45^\circ$, the frequency is $\nu = 2 \text{ CPD} * \sin(\phi) = 1.42 \text{ CPD}$.

We follow the spectral analysis of Wheeler and Kiladis (1999) by cutting the time series into non-overlapping segments for the different seasons, and average the segments from the different years. The use of non-overlapping seasonal segments permits exploration of seasonal dependence in the signals and is justified because the waves of interests about have periods much shorter than a season. Weak signals are revealed by summing over the 40 segments of each season, increasing the statistical significance of the spectral analysis. Linear trends are removed from each segment, and then tapering windows are applied in the (non-periodic) latitudinal and time dimensions of the data. We use the standard cosine-tapered Tukey window with $\alpha=0.5$ to reduce spectral leakage (Prabhu 2014). After the data has been pre-processed as described above, we perform a 3-dimensional complex discrete Fourier transform on both the geopotential height (h) and the horizontal components of the wind velocity (v), so that cross-correlations can be computed in the frequency-wavevector space. The gauge-invariant complex-valued cross-correlation field in frequency - zonal wavenumber - meridional wavenumber space is then formed by multiplying the complex-conjugate of the Fourier-transformed geopotential height against the horizontal components of the wind velocity. We denote these quantities as $\langle h(\vec{k}; \nu) | u(\vec{k}; \nu) \rangle$ and $\langle h(\vec{k}; \nu) | v(\vec{k}; \nu) \rangle$ where the brackets indicate the processing steps described above. The complex field $\langle h(\vec{k}; \nu) | v(\vec{k}; \nu) \rangle$ should be compared to the theoretical calculation of Ξ as defined by Eq. 4 and theory predicts that $\langle h(\vec{k}; \nu) | u(\vec{k}; \nu) \rangle$ will show similar topology. After selecting a particular frequency, the complex-valued data in the two-dimensional k - ℓ space is averaged over a moving Gaussian spectral window to further improve statistical significance (albeit at the cost of reduced spectral resolution). The Gaussian window here is treating the wavevector space pattern as an image and has the standard deviation $\sigma = 1.5$ the spacing between points in wavevector space. Finally the magnitude and phase of the complex-valued fields $\langle h(\vec{k}; \nu) | u(\vec{k}; \nu) \rangle$ and $\langle h(\vec{k}; \nu) | v(\vec{k}; \nu) \rangle$ are visualized with vectors in horizontal wavevector space. Matlab code that implements this algorithm is presented in the Appendix.

4. Results

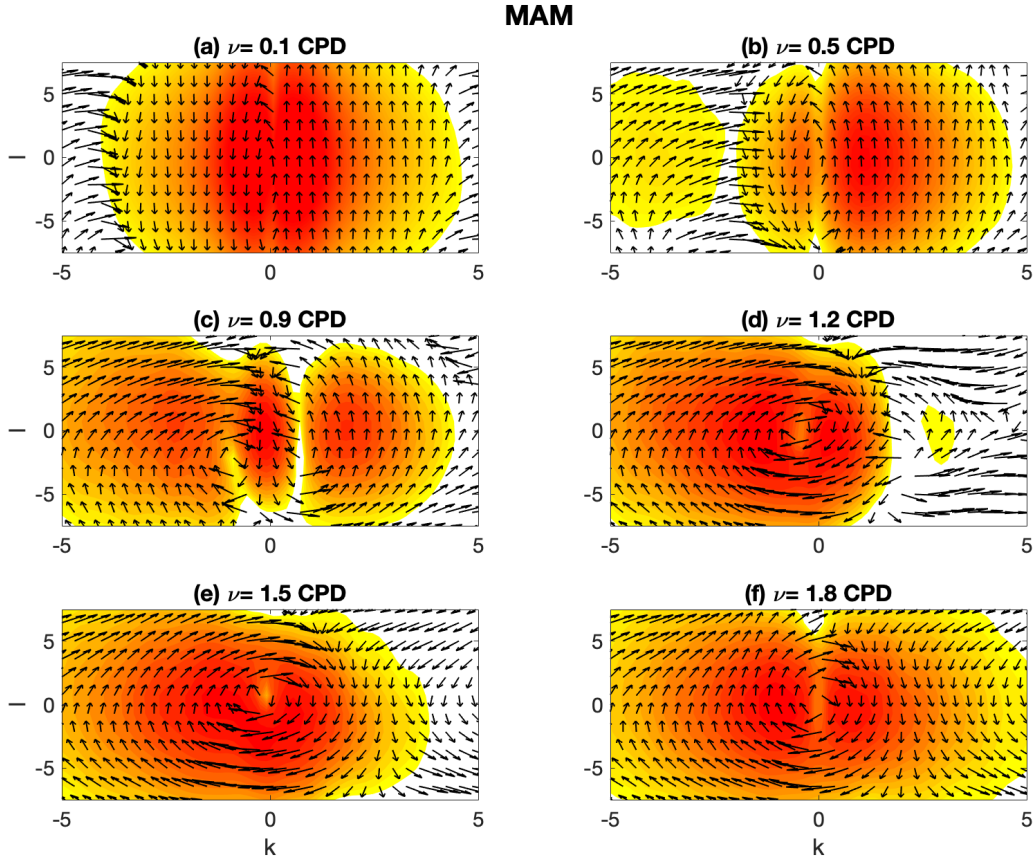
We turn first to the power spectra of the meridional component of the wind velocity and the geopotential height to verify that power can be found in the expected regions of frequency - wavevector space. We average the power spectra over meridional wavenumbers (ℓ). Fig. 3 shows the power in zonal wavenumber (k) - frequency (ν) space. Apparent is the sharp signal at $\nu = 1$ CPD due to the diurnal cycle as well as a semi-diurnal harmonic. High-frequency Poincaré-gravity waves are separated by a gap in the power from low-frequency planetary waves as expected, and exhibit more power in the $k < 0$ region (Wheeler and Kiladis 1999). The peak in the low-frequency waves at $k > 0$ corresponds to eastward planetary waves whereas part of the signal for $k < 0$ is due to standing waves that contribute equally to both positive and negative zonal wavenumbers. However it is also clear that the spectra are far from the dispersion of the idealized rotating shallow-water dispersion shown in Figure 1.



42 FIG. 3. The 50 hPa power spectra of meridional velocity (v) and geopotential height (h) in the zonal wavenumber
 43 (k) - frequency (ν) space over latitudes 25°N to 65°N . The frequency ν has units of cycles per day (CPD), and k
 44 has the unit of cycles per circumference.

The winding number is discerned by plotting the cross-correlations $\langle h(\vec{k}; \nu) | u(\vec{k}; \nu) \rangle$ and $\langle h(\vec{k}; \nu) | v(\vec{k}; \nu) \rangle$ in k - ℓ wavevector space. From Fig. 2, we expect Poincaré-gravity waves in the northern hemisphere to have a vortex pattern with winding number = +1 at large positive frequencies. By contrast planetary waves will be topologically trivial with a domain wall. Fig. 4 shows that the observational data displays these topological properties. Vortices with winding

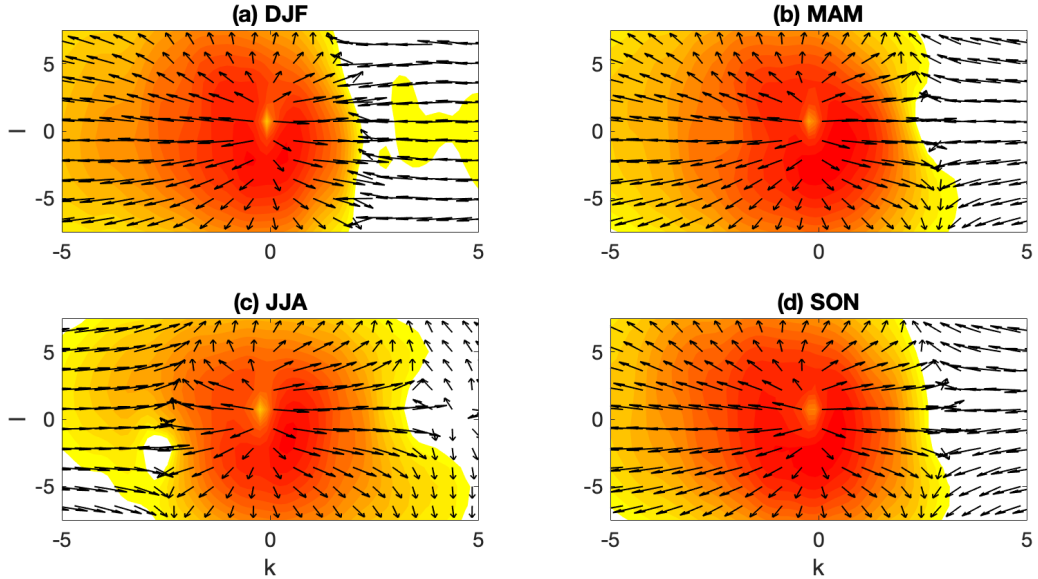
number equal to +1 appear at frequencies larger in magnitude than 1 CPD, consistent with the theoretical expectation for Poincaré waves. At lower frequencies there are no vortices; instead a



45 FIG. 4. The cross-correlation $\langle h(\vec{k}; \nu) | \nu(\vec{k}; \nu) \rangle$ for the spring season (March, April, May) obtained from
 46 ERA5 data for the region 25°N-65°N at 50 hPa. Subplots are at different frequencies ν . Colors represent the
 47 magnitude $|\langle h(\vec{k}; \nu) | \nu(\vec{k}; \nu) \rangle|$ on a logarithmic scale with white = zero, and arrows represent the phase (argument)
 48 of $\langle h(\vec{k}; \nu) | \nu(\vec{k}; \nu) \rangle$.

topologically-trivial domain wall appears in qualitative agreement with the prediction for Rossby waves, with the phase reversing by 180° upon passing through zonal wavenumber $k = 0$.

There are some small seasonal variations in the patterns of the Poincaré waves (Fig. 5). We note that the vortex center is offset slightly from the origin in wavevector space. The offset could be explained by the mean background state flow which varies with season but further investigation is required. Lower down in the lower troposphere at 850 hPa the Rossby wave pattern persists as



49 FIG. 5. Cross-correlation between $\langle h(\vec{k}; \nu) | u(\vec{k}; \nu) \rangle$ obtained from ERA5 data for the region $25^\circ\text{N} - 65^\circ\text{N}$ at
 50 50 hPa at frequency $\nu = 1.5$ CPD for the different seasons.

expected but the high frequency patterns are no longer coherent (Fig. 6). The atmosphere is not strongly stratified and macroturbulence in the form of jets and synoptic scale weather dominates the signal obscuring any gravity waves. Although vortices are no longer evident, we note that the high-frequency correlations are strongest in magnitude at positive zonal wavenumbers.

5. Conclusion

In this paper we demonstrate that Poincaré-gravity waves in the stratosphere have the non-trivial topological signature expected from theoretical prediction. This work reverses the standard chain of reasoning that begins from the observed dispersion to deduce the existence of equatorial Kelvin and Yanai waves. From the existence of these waves, the non-trivial topology of the Poincaré-gravity waves away from the equator is then inferred from the principle of bulk-interface correspondence and found to agree with theory (Delplace et al. 2017). Here by contrast we directly interrogate the topology of the superinertial gravity waves away from the equator using ERA5 reanalysis data at 50 hPa pressure level. We find the theoretically expected winding number of +1 at higher frequency. The topological signature of Poincaré-gravity waves is clear despite the fact

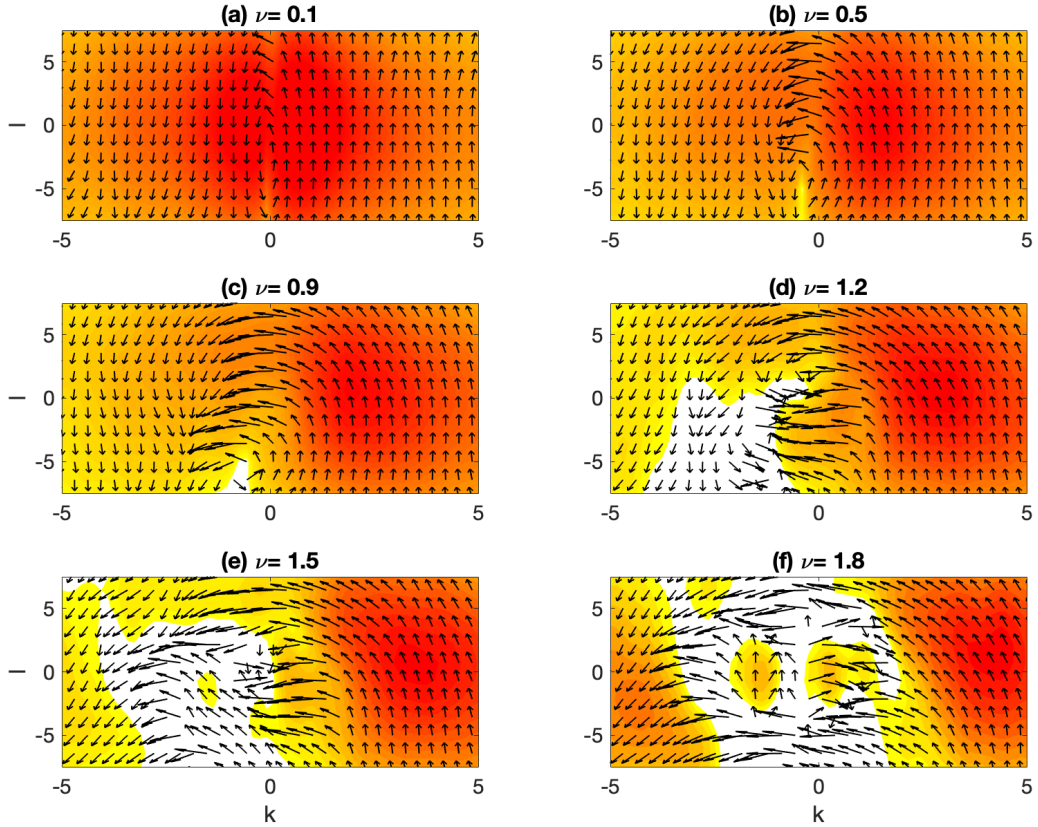


FIG. 6. Same as Fig.4, but for an altitude of 850 hPa.

that their dispersion relation cannot be clearly discerned in power spectra. The winding number vanishes at low frequencies and the low-frequency planetary waves have trivial topology that can be plainly distinguished from the Poincaré-gravity waves. The non-trivial topological signature of the superinertial gravity waves also disappears in the lower troposphere reflecting the absence of stable stratification.

A shortcoming of the approach described here is that it requires data fields that are well-resolved in both wavevector and (high) frequency space, ruling out the use of spatially sparse data. However it may be possible to work directly in real space instead of wavevector space (while remaining in frequency space): A spatial Fourier transform of $\Xi_{\pm}(k, \ell)$ (Eq. 5) shows that $\Xi_{\pm}(x, y)$ too displays a vortex. It may be possible to detect the vortex in spatially-sparse buoy data provided that the

sampling rate is sufficiently high to capture superinertial frequencies. We leave this for future work.

The mathematics of topology has great predictive power because it makes complicated problems simple by focusing on robust features. The topology we investigate here plays out in frequency-wavevector space, rather than in real space. Topology in this setting is a new tool for climate science that is relatively immune to background noise as the distinct signatures of topology found in ERA5 observations of Poincaré-gravity waves qualitatively distinguish them from planetary waves. Future application to emergent wavelike phenomena such as the Madden-Julian Oscillation may be envisioned.

Acknowledgments. We thank Tamara Barriquand, George Kiladis, Dung Nguyen, and Antoine Venaille for helpful discussions. This work was supported in part by a grant from the Institute at Brown for Environment and Society and by a grant from the Simons Foundation (Grant number 662962, GF). It was performed in part at Aspen Center for Physics, which is supported by National Science Foundation grant PHY-2210452. Z.Z. is supported by a Stanford Science fellowship.

Data availability statement. The ERA5 reanalysis wind and geopotential height data is provided by the Copernicus Climate Change Service (C3S) at ECMWF (<https://www.ecmwf.int/en/forecasts/dataset/ecmwf-reanalysis-v5>, accessed on 14 April 2022).

References

- Bouteyre, P., and Coauthors, 2022: Non-Hermitian topological invariant of photonic band structures undergoing inversion. *arXiv:2211.09884*, <https://doi.org/10.48550/arxiv.2211.09884>, 2211.09884.
- Delplace, P., J. B. Marston, and A. Venaille, 2017: Topological origin of equatorial waves. *Science*, **358** (6366), 1075–1077, <https://doi.org/10.1126/science.aan8819>, URL <https://www.science.org/doi/full/10.1126/science.aan8819>.
- Farrar, J. T., 2008: Observations of the dispersion characteristics and meridional sea level structure of equatorial waves in the Pacific Ocean. *Journal of physical oceanography*, **38** (8), 1669–1689, <https://doi.org/10.1175/2007JPO3890.1>, URL <https://doi.org/10.1175/2007JPO3890.1>.
- Hasan, M. Z., and C. L. Kane, 2010: Colloquium: Topological insulators. *Rev. Mod. Phys.*, **82** (4), 3045–3067, <https://doi.org/10.1103/RevModPhys.82.3045>, URL <https://link.aps.org/doi/10.1103/RevModPhys.82.3045>.
- Hendershott, M., and W. Munk, 1970: Tides. *Annual review of fluid mechanics*, **2** (1), 205–224, publisher: Annual Reviews 4139 El Camino Way, PO Box 10139, Palo Alto, CA 94303-0139, USA.
- Hersbach, H., and Coauthors, 2020: The ERA5 global reanalysis. *Quarterly Journal of the Royal Meteorological Society*, **146** (730), 1999–2049, <https://doi.org/10.1002/qj.3803>, URL <https://onlinelibrary.wiley.com/doi/abs/10.1002/qj.3803>.

- Horsley, S. A. R., 2022: Tutorial: Topology, waves, and the refractive index. *arXiv:2202.08643*, <https://doi.org/10.48550/arxiv.2202.08643>.
- Hoskins, B. J., M. E. McIntyre, and A. W. Robertson, 1985: On the use and significance of isentropic potential vorticity maps. *Quarterly Journal of the Royal Meteorological Society*, **111 (470)**, 877–946.
- Madden, R. A., and P. R. Julian, 1971: Detection of a 40 – 50 day oscillation in the zonal wind in the tropical Pacific. *Journal of Atmospheric Sciences*, **28 (5)**, 702–708.
- Pahlavan, H. A., J. M. Wallace, Q. Fu, and G. N. Kiladis, 2021: Revisiting the Quasi-Biennial Oscillation as Seen in ERA5. Part II: Evaluation of Waves and Wave Forcing. *Journal of the Atmospheric Sciences*, **78 (3)**, 693–707, <https://doi.org/10.1175/JAS-D-20-0249.1>, URL <https://journals.ametsoc.org/view/journals/atsc/78/3/JAS-D-20-0249.1.xml>.
- Prabhu, K. M. M., 2014: *Window Functions and Their Applications in Signal Processing*. Taylor & Francis, <https://doi.org/10.1201/9781315216386>, URL <https://library.oapen.org/handle/20.500.12657/41686>.
- Renteln, P., 2013: *Manifolds, Tensors, and Forms: An Introduction for Mathematicians and Physicists*. Cambridge University Press, URL <https://books.google.com/books?id=uJWGAgAAQBAJ>.
- Venaille, A., and P. Delplace, 2021: Wave topology brought to the coast. *Physical Review Research*, **3 (4)**, 043 002, <https://doi.org/10.1103/physrevresearch.3.043002>, 2011.03440.
- Wheeler, M., and G. N. Kiladis, 1999: Convectively Coupled Equatorial Waves: Analysis of Clouds and Temperature in the Wavenumber – Frequency Domain. *Journal of the Atmospheric Sciences*, **56 (3)**, 374–399, [https://doi.org/10.1175/1520-0469\(1999\)056<0374:CCEWAO>2.0.CO;2](https://doi.org/10.1175/1520-0469(1999)056<0374:CCEWAO>2.0.CO;2), URL https://journals.ametsoc.org/view/journals/atsc/56/3/1520-0469_1999_056_0374_ccewao_2.0.co_2.xml.
- Wyrtki, K., 1975: El Niño – the dynamic response of the equatorial Pacific Ocean to atmospheric forcing. *Journal of Physical Oceanography*, **5 (4)**, 572–584.
- Zhu, Z., C. Li, and J. Marston, 2021: Topology of rotating stratified fluids with and without background shear flow. *arXiv:2112.04691*, <https://doi.org/10.48550/arxiv.2112.04691>.

APPENDIX

MATLAB Code for Cross-Spectrum Calculation

```
1  %%%%%%%%%%% Read Data %%%%%%%%%%%
2  clear
3  fname='V.ERA.nc';
4  readncfile
5  fname='Z.ERA.nc';
6  readncfile
7
8  %%%%%%%%%%% Lower Spatial Resolution %%%%%%%%%%%
9  lat1=linspace(25,65,41).';
10 long1=linspace(-180,180,145).';
11
12 %%
13 [X,Y]=meshgrid(longitude,latitude);
14 [X1,Y1]=meshgrid(long1(1:144),lat1(1:40));
15
16 %%
17 for i=1:length(time)
18     v1(:,:,i)=interp2(X,Y,squeeze(v(:,:,i)).',X1,Y1);
19     z1(:,:,i)=interp2(X,Y,squeeze(z(:,:,i)).',X1,Y1);
20 end
21
22 %%%%%%%%%%% Filter Out Low-Frequency Signals %%%%%%%%%%%
23 for i=1:40
24     i
25     for j=1:144
26         cv=squeeze(v1(i,j,:));
27         fx_v=vfilt(cv,ones(182,1)./182,'mirror');
28         resv=cv-fx_v;
29         vano(i,j,:)=resv;
30
31         cz=squeeze(z1(i,j,:));
32         fx_z=vfilt(cz,ones(182,1)./182,'mirror');
33         resz=cz-fx_z;
```

```

34         zano(i,j,:)=resz;
35     end
36 end
37
38 %%%%%%%%%%% Divide into Segments of seasons %%%%%%%%%%%
39 monthday=[31,28,31,30,31,30,31,31,30,31,30,31];
40 yearday=cumsum(monthday);
41
42 for i=1:40
43     segment_v(i,:,:)=v1(:,:, (i-1)*365*4+yearday(2)*4+1:(i-1)*365*4+yearday(5)*4);
44     segment_z(i,:,:)=z1(:,:, (i-1)*365*4+yearday(2)*4+1:(i-1)*365*4+yearday(5)*4);
45 end % here is MAM for example
46
47 [k1,k2,k3,k4]=size(segment_v);
48 %%
49
50 %%%%%%%%%%% Taper %%%%%%%%%%%
51 %% Tapering in time dimension %%
52 time1=1/4:1/4:92;
53 n=length(time1);
54 w=tukeywin(n);
55 for i=1:k1
56     for j=1:k2
57         for k=1:k3
58             y_v=squeeze(segment_v(i,j,k,:));
59             b_v=time1.\y_v;
60             ymean_v=time1.*b_v;
61             vanod(i,j,k,:)=(y_v-ymean_v).*w;
62
63             y_z=squeeze(segment_z(i,j,k,:));
64             b_z=time1.\y_z;
65             ymean_z=time1.*b_z;
66             zanod(i,j,k,:)=(y_z-ymean_z).*w;
67         end
68     end
69 end
70 %%
71 %% Tapering in meridional dimension %%

```

```

72 nlat=k2;
73 w1=tukeywin(nlat);
74 for i=1:k1
75     i
76     for j=1:k4
77         for k=1:k3
78             vanod1(i, :, k, j)=squeeze(vanod(i, :, k, j)).'*w1;
79             zanod1(i, :, k, j)=squeeze(zanod(i, :, k, j)).'*w1;
80         end
81     end
82 end
83
84 %%
85 %%%%%%%%%%%%%%%%%%%%%%%%%%%%%%%%%%%%%%%%%%%%%%%%%%%%%%%%%%%%%%%%%%%%%%%%% 3-D Fourier Transform %%%%%%%%%%%%%%%%%%%%%%%%%%%%%%%%%%%%%%%%%%%%%%%%%%%%%%%%%%%%%%%%%%%%%%%%%
86 for i=1:k1
87     spec_v(i, :, :, :)=fftshift(fftshift(fftshift(squeeze(vanod1(i, :, :, :))))/k2/k3/k4);
88     spec_z(i, :, :, :)=fftshift(fftshift(fftshift(squeeze(zanod1(i, :, :, :))))/k2/k3/k4);
89 end
90
91 %%
92 %%%%%%%%%%%%%%%%%%%%%%%%%%%%%%%%%%%%%%%%%%%%%%%%%%%%%%%%%%%%%%%%%%%%%%%%% Calculate Cross-Spectrum %%%%%%%%%%%%%%%%%%%%%%%%%%%%%%%%%%%%%%%%%%%%%%%%%%%%%%%%%%%%%%%%%%%%%%%%%
93 pi=3.1415926536;
94 dt=1/4;
95 dx=2*pi/144;
96 dy=pi/180;
97
98 df=1./k4./dt;
99 dkx=1./k3./dx;
100 dky=1./k2./dy;
101
102 spec_cross=spec_v.*conj(spec_z)./df./dkx./dky;
103
104 %%%%%%%%%%%%%%%%%%%%%%%%%%%%%%%%%%%%%%%%%%%%%%%%%%%%%%%%%%%%%%%%%%%%%%%%% Visualize %%%%%%%%%%%%%%%%%%%%%%%%%%%%%%%%%%%%%%%%%%%%%%%%%%%%%%%%%%%%%%%%%%%%%%%%%
105 f=[-fliplr(1:(k4/2)) 0 (1:(k4/2-1))].*df;
106
107 kx=[-fliplr(1:(k3/2))+0.5 (1:(k3/2))-0.5].*dkx;
108 ky=[-fliplr(1:(k2/2))+0.5 (1:(k2/2))-0.5].*dky;
109

```

```

110 %% Find corresponding frequencies, sum up segments %%
111 crossxy_1=squeeze(sum(spec_cross(:, :, :, 176), 1));
112 crossxy_5=squeeze(sum(spec_cross(:, :, :, 139), 1));
113 crossxy_9=squeeze(sum(spec_cross(:, :, :, 102), 1));
114 crossxy_12=squeeze(sum(spec_cross(:, :, :, 75), 1));
115 crossxy_15=squeeze(sum(spec_cross(:, :, :, 47), 1));
116 crossxy_18=squeeze(sum(spec_cross(:, :, :, 19), 1));
117
118
119 h = fspecial('gaussian', [k2 k3], 1.5);
120 result_1 = imfilter(crossxy_1, h, 'replicate');
121 result_5 = imfilter(crossxy_5, h, 'replicate');
122 result_9 = imfilter(crossxy_9, h, 'replicate');
123 result_12 = imfilter(crossxy_12, h, 'replicate');
124 result_15 = imfilter(crossxy_15, h, 'replicate');
125 result_18 = imfilter(crossxy_18, h, 'replicate');
126
127
128 gapkx=2;
129 gapky=1;
130 kx1=kx(1:gapkx:k3);
131 ky1=ky(1:gapky:k2);
132 result1_1=result_1(1:gapky:k2, 1:gapkx:k3);
133 result1_5=result_5(1:gapky:k2, 1:gapkx:k3);
134 result1_9=result_9(1:gapky:k2, 1:gapkx:k3);
135 result1_12=result_12(1:gapky:k2, 1:gapkx:k3);
136 result1_15=result_15(1:gapky:k2, 1:gapkx:k3);
137 result1_18=result_18(1:gapky:k2, 1:gapkx:k3);
138
139 avgphi3_1=angle(result1_1);
140 avgphi3_5=angle(result1_5);
141 avgphi3_9=angle(result1_9);
142 avgphi3_12=angle(result1_12);
143 avgphi3_15=angle(result1_15);
144 avgphi3_18=angle(result1_18);
145
146
147 %%%%%%%%%%%%%%%%%%%%%%%%%%%%%%%%%%%%%%%%%%%%%%%%%%%%%%%%%%%%%%%%%%%%%%%%%

```

```

148
149 f=figure;
150 f.Position(3:4) = [900 660];
151 quiversize=0.6;
152 color='k';
153
154 xlimrange=[-5 5];
155 ylimrange=[-7.5 7.5];
156
157 subplot(3,2,1)
158 clims=-1:0.1:3;
159 contourf(kx,ky,log10(abs(result_1)),clims,'LineStyle','none');
160 %,clims
161 title('(a) \nu= 0.1 CPD')
162 xlim(xlimrange)
163 ylim(ylimrange)
164 ylabel('l')
165 set(gca,'FontSize',15)
166 colormap(flipud(autumn))
167 hold on
168
169 quiver(kx1,ky1,cos(avgphi3-1),sin(avgphi3-1),quiversize,color,'LineWidth',1)
170
171 %%%%%%%%%%%%%%%%%%%%%%%%%%%%%%%%%%%%%%%%%%%%%%%%%%%%%%%%%%%%%%%%%%%%%%%%%
172 subplot(3,2,2)
173 contourf(kx,ky,log10(abs(result_5)),clims,'LineStyle','none');
174 %,clims
175 title('(b) \nu= 0.5 CPD')
176 xlim(xlimrange)
177 ylim(ylimrange)
178 set(gca,'FontSize',15)
179 colormap(flipud(autumn))
180 hold on
181
182 quiver(kx1,ky1,cos(avgphi3-5),sin(avgphi3-5),quiversize,color,'LineWidth',1)
183
184 %%%%%%%%%%%%%%%%%%%%%%%%%%%%%%%%%%%%%%%%%%%%%%%%%%%%%%%%%%%%%%%%%%%%%%%%%
185

```

```

186 subplot(3,2,3)
187 contourf(kx,ky,log10(abs(result_9)),clims,'LineStyle','none');
188 %,clims
189 title('(c) \nu= 0.9 CPD')
190 xlim(xlimrange)
191 ylim(ylimrange)
192 ylabel('l')
193 set(gca,'FontSize',15)
194 colormap(flipud(autumn))
195 hold on
196
197 quiver(kx1,ky1,cos(avgphi3_9),sin(avgphi3_9),quiversize,color,'LineWidth',1)
198
199 %%%%%%%%%%%%%%%%%%%%%%%%%%%%%%%%%%%%%%%%%%%%%%%%%%%%%%%%%%%%%%%%%%%%%%%%%
200
201 subplot(3,2,4)
202 contourf(kx,ky,log10(abs(result_12)),clims,'LineStyle','none');
203 %,clims
204 title('(d) \nu= 1.2 CPD')
205 xlim(xlimrange)
206 ylim(ylimrange)
207 set(gca,'FontSize',15)
208 colormap(flipud(autumn))
209 hold on
210
211 quiver(kx1,ky1,cos(avgphi3_12),sin(avgphi3_12),quiversize,color,'LineWidth',1)
212
213 %%%%%%%%%%%%%%%%%%%%%%%%%%%%%%%%%%%%%%%%%%%%%%%%%%%%%%%%%%%%%%%%%%%%%%%%%
214 subplot(3,2,5)
215 contourf(kx,ky,log10(abs(result_15)),clims,'LineStyle','none');
216 %,clims
217 title('(e) \nu= 1.5 CPD')
218 xlim(xlimrange)
219 ylim(ylimrange)
220 xlabel('k')
221 ylabel('l')
222 set(gca,'FontSize',15)
223 colormap(flipud(autumn))

```



```

224 hold on
225
226 quiver(kx1,ky1,cos(avgphi3_15),sin(avgphi3_15),quiversize,color,'LineWidth',1)
227
228 %%%%%%%%%%%%%%%%%%%%%%%%%%%%%%%%%%%%%%%%%%%%%%%%%%%%%%%%%%%%%%%%%%%%%%%%%
229
230 subplot(3,2,6)
231 contourf(kx,ky,log10(abs(result_18)),clims,'LineStyle','none');
232 %,clims
233 title('(f) \nu= 1.8 CPD')
234 xlim(xlimrange)
235 ylim(ylimrange)
236 xlabel('k')
237 set(gca,'FontSize',15)
238 colormap(flipud(autumn))
239 hold on
240
241 quiver(kx1,ky1,cos(avgphi3_18),sin(avgphi3_18),quiversize,color,'LineWidth',1)

```